Synthesis and Thermoelectric Properties of Yb-doped $Ca_{0.9-x}Yb_xLa_{0.1}MnO_3$ Ceramics

BO ZHANG,[1,2,3] AIMIN CHANG,[2,5] QING ZHAO,[2] HAITAO YE,[4] and YIQUAN WU[1,6]

1.—Kazuo Inamori School of Engineering, New York State College of Ceramics at Alfred University, Alfred, NY 14802, USA. 2.—Xinjiang Key Laboratory of Electronic Information Materials and Devices, Key Laboratory of Functional Materials and Devices Under Special Environments of CAS, Xinjiang Technical Institute of Physics and Chemistry of CAS, Urumqi 830011, China. 3.—University of Chinese Academy of Sciences, Beijing 100049, China. 4.—School of Engineering and Applied Science, Aston University, Birmingham B4-7ET, UK. 5.—e-mail: changam@ms.xjb.ac.cn. 6.—e-mail: wuy@alfred.edu

The microstructure and thermoelectric properties of Yb-doped $Ca_{0.9-x}Yb_xLa_{0.1}MnO_3$ ($0 \leq x \leq 0.05$) ceramics prepared by using the Pechini method derived powders have been investigated. X-ray diffraction analysis has shown that all samples exhibit single phase with orthorhombic perovskite structure. All ceramic samples possess high relative densities, ranging from 97.04% to 98.65%. The Seebeck coefficient is negative, indicating n-type conduction in all samples. The substitution of Yb for Ca leads to a marked decrease in the electrical resistivity, along with a moderate decrease in the absolute value of the Seebeck coefficient. The highest power factor is obtained for the sample with $x = 0.05$. The electrical conduction in these compounds is due to electrons hopping between Mn^{3+} and Mn^{4+}, which is enhanced by increasing Yb content.

Key words: Manganites, Pechini method, power factor, electrical conduction

INTRODUCTION

Thermoelectric (TE) materials, which allow for the direct conversion of heat or unused waste heat into electric energy and vice versa, have recently received much interest for use in clean energy sources and device cooling applications.[1,2] The energy conversion performance of TE materials is characterized by the figure of merit $ZT = S^2T/\rho\kappa$, where S, ρ, and κ are the thermopower or Seebeck coefficient, electrical resistivity, and thermal conductivity, respectively. To be a TE material of high efficiency, the material must have a large Seebeck coefficient, a low resistivity, and a low thermal conductivity. However, these three physical parameters are dependent upon each other because they are all related to the scattering mechanisms of charge carriers and lattice vibrations,[3] thus obtaining the optimization of TE performance requires a compromise between them.

Recently, perovskite-type manganites have received extensive attention due to their interesting properties such as superconductivity, magnetism, colossal magnetoresistance (CMR), orbital ordering (OO), charge ordering (CO) and phase-separation, etc.[4,5] Among perovskites, $CaMnO_3$ and electron-doped $CaMnO_3$ perovskite solid solutions have been found to be very interesting because of their high temperature TE performance. $CaMnO_3$, with an orthorhombic perovskite structure, is an n-type semiconductor without e_g electrons, and exhibits G-type antiferromagnetism below $T_N = 120$ K as well as a large resistivity.[5] Doping with electrons introduces mobile electrons into the e_g band and thus the interaction of these carriers via t_{2g} spins induces changes in the electrical properties.[6] Therefore, the electrical conductivity of $CaMnO_3$ can be easily improved by the substitution for both Mn and Ca sites, while the effect of cation substitution on electrical and TE properties of $CaMnO_3$

$$\boxed{\begin{array}{c} La(NO_3)_2 \cdot 6H_2O + Ca(NO_3)_2 \cdot 4H_2O \\ Mn(NO_3)_2 \cdot 4H_2O + Yb(NO_3)_2 \cdot 5H_2O + H_2O \end{array}} \quad \boxed{C_6H_8O_7 + C_2H_6O_2 + H_2O}$$

Stirring for 1 h

$$\boxed{\text{Solution}}$$

Heating at 90 °C

$$\boxed{\text{Gel}}$$

Drying at 150 °C

$$\boxed{\text{Dried powder}}$$

Decomposing at 500 °C and
then calcining at 900 °C

$$\boxed{\text{Powder}}$$

$$\boxed{\text{Pressing into disk}}$$

Cold isostatic pressing
at 140 MPa and then
sintering at 1300 °C

$$\boxed{\text{Bulk ceramics}}$$
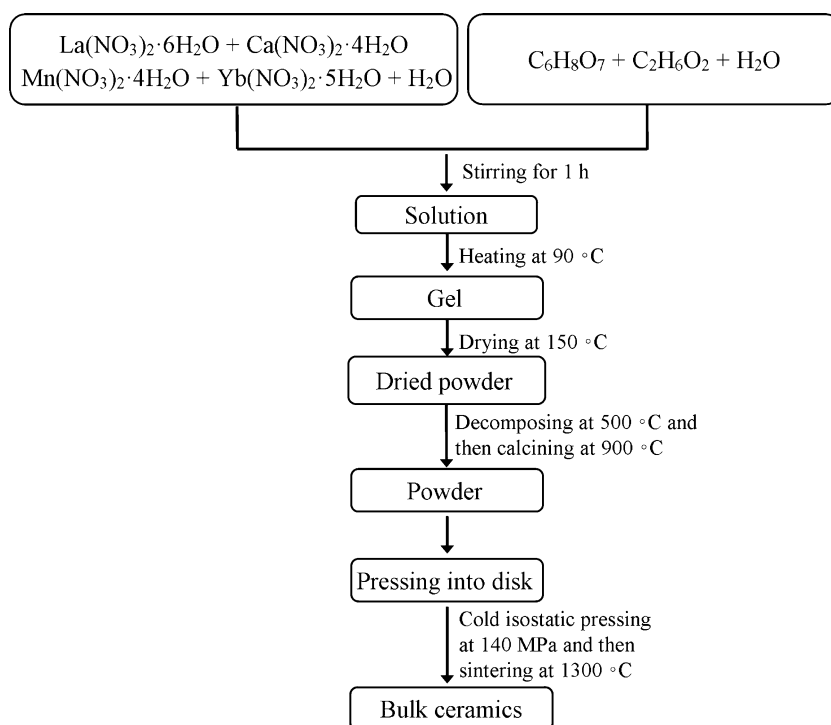
Fig. 1. Flow chart for the fabrication of $Ca_{0.9-x}Yb_xLa_{0.1}MnO_3$ ($0 \leq x \leq 0.05$) ceramics.

has been studied previously.[3–12] In particular, lightly electron-doped $CaMnO_3$ has a much lower resistivity than un-doped $CaMnO_3$, but still possesses a relatively high thermopower, and thus exhibits good TE performance.[5] To give an example, La-doped $CaMnO_3$ ceramics lead to a significant increase in electrical conductivity of 2–4 orders of magnitude.[10] Hideki Taguchi has studied the TE properties of $Ca_{1-x}La_xMnO_3$ ceramics.[7] A $Ca_{0.96}La_{0.04}MnO_3$ sample synthesized through a polymerized complex method has the highest value for the power factor (S^2/ρ) 3–4 $\times 10^{-4}$ W/(K^{2}m).[7] The TE properties of $Ca_{1-x}R_xMnO_3$ (R = La, Y and Ce) perovskite ceramics have also been investigated.[11] It was found that the optimal electron concentration is around 0.1–0.12 for TE performance and the ZT value of $Ca_{0.9}La_{0.1}MnO_3$ exceeds 0.12 at 1000 K, which exhibits potential as a good high temperature TE material. On the other hand, Yb-doped $CaMnO_3$ results in a higher electrical conductivity and Seebeck coefficient, which causes a larger figure of merit.[9] Samples of $Ca_{0.9}Yb_{0.1}MnO_3$ are reported to show ZT values as high as 0.2 at 1000 K, making it another promising high temperature TE material.[12]

Based on the effects of Yb and La single doping in the above description, the secondary element Yb will be introduced in $Ca_{0.9}La_{0.1}MnO_3$ ceramics, and is expected to improve their power factor. Recently, the Pechini method based on sol–gel technology has been attempted for the preparation of the perovskite oxide powders because it can avoid contaminating the final powder, and also leads to a homogeneous,

highly reactive powder.[13,14] In this study, the series of Yb-doped $Ca_{0.9-x}Yb_xLa_{0.1}MnO_3$ were prepared by the Pechini method to investigate the effect of the Yb content on the structure, microstructure, and TE properties. At the same time, the relationship between resistivity and Yb contents was quantitatively analyzed by using x-ray photoelectron spectroscopy.

EXPERIMENTAL PROCEDURE

$Ca_{0.9-x}Yb_xLa_{0.1}MnO_3$ (x = 0, 0.01, 0.03, 0.05) powders were synthesized using the Pechini method.[15] Appropriate amounts of $La(NO_3)_3 \cdot 6H_2O$, $Mn(NO_3)_2 \cdot 4H_2O$, $Yb(NO_3)_3 \cdot 5H_2O$, and $Ca(NO_3)_2 \cdot 4H_2O$ were first dissolved into distilled water. Then, the citric acid dissolved into distilled water and ethylene glycol were slowly added in the above solution and homogenized through the use of magnetic stirring for 1 h. The molar ratio of citric acid, ethylene glycol, and metal ions was 1.2:1.2:1. The mixture solution was then heated at 90°C on a hot plate with continuous stirring for dehydration, resulting in the formation of a gel. A loose powder was obtained after the gel was dried at 150°C for approximately 2 days. The dried powders were ground in a mortar and decomposed in air at 500°C for 1 h. The powders were then ground and calcined at 900°C for 6 h. The calcined powders were then ground again and pressed into disks at a die pressure of 20 MPa. Cold isostatic pressing at 140 MPa was used to enhance the green density of the compact. The pressed green disks were sintered in air at 1300°C for

4 h. Figure 1 shows the flow chart for the fabrication of $Ca_{0.9-x}Yb_xLa_{0.1}MnO_3$ ceramics.

The ceramic density was determined by the Archimedes method. The thermal decomposition behavior of the gels was characterized by thermogravimetric and differential thermal analysis (TG/DTA; SDT 2980-TA Instruments) in air atmosphere with a flow rate of 100 mL/min and at a heating rate of 10°C/min up to 1000°C. X-ray diffraction (XRD; Bruker D2-ADVANCE) using CuK_α radiation was used to identify crystalline phases in the calcined powders and sintered ceramics. The microstructures of the sintered ceramics were observed using a scanning electron microscope (SEM; FEI Quanta 200). X-ray photoelectron spectroscopy (XPS; Thermo Fisher, ESCALAB 250) was used to analyze the chemical states of the sintered ceramics.

The sintered pellets were cut into rectangular bars with dimensions of 5 mm × 2 mm × 15 mm to measure resistivity and the Seebeck coefficient. Then, the rectangular bars were polished, coated with a thin layer of non-fluxed Pt paste, and heated to 900°C for 30 min. The resistivity and Seebeck coefficient were measured simultaneously in air from 100°C to 600°C using a custom-made computer-controlled system that includes a current source (Model 2400; Keithley Instruments, USA) and a digital multimeter (Model 2700; Keithely Instruments) based on the four-point steady state gradient technique.[16] The Seebeck coefficient was obtained from the slope of the linear relationship between ΔV and ΔT, where ΔV is the TE voltage produced by the temperature gradient ΔT.

RESULTS AND DISCUSSION

TG/DTA Analysis

Figure 2 shows the TG–DTA curves of $Ca_{0.9-x}Yb_xLa_{0.1}MnO_3$ gels from room temperature to 1000°C. For all the DTA curves, the upward peaks are exothermic. All the TG plots show two major losses in the temperature ranges 25–200°C and 200–500°C. The initial weight loss below 200°C may be due to the evaporation and desorption of the solvent molecules. The second and the most significant weight loss may be attributed to the reaction of nitrates with citric acid and the burnout of the residual organic species. This observation can be confirmed by the three exothermic peaks from 200°C to 500°C in the DTA curves. During the exothermic reaction, large amounts of gases such as H_2O, CO_2 and N_2 were released, resulting in a significant weight loss in the TG plots. Additionally,
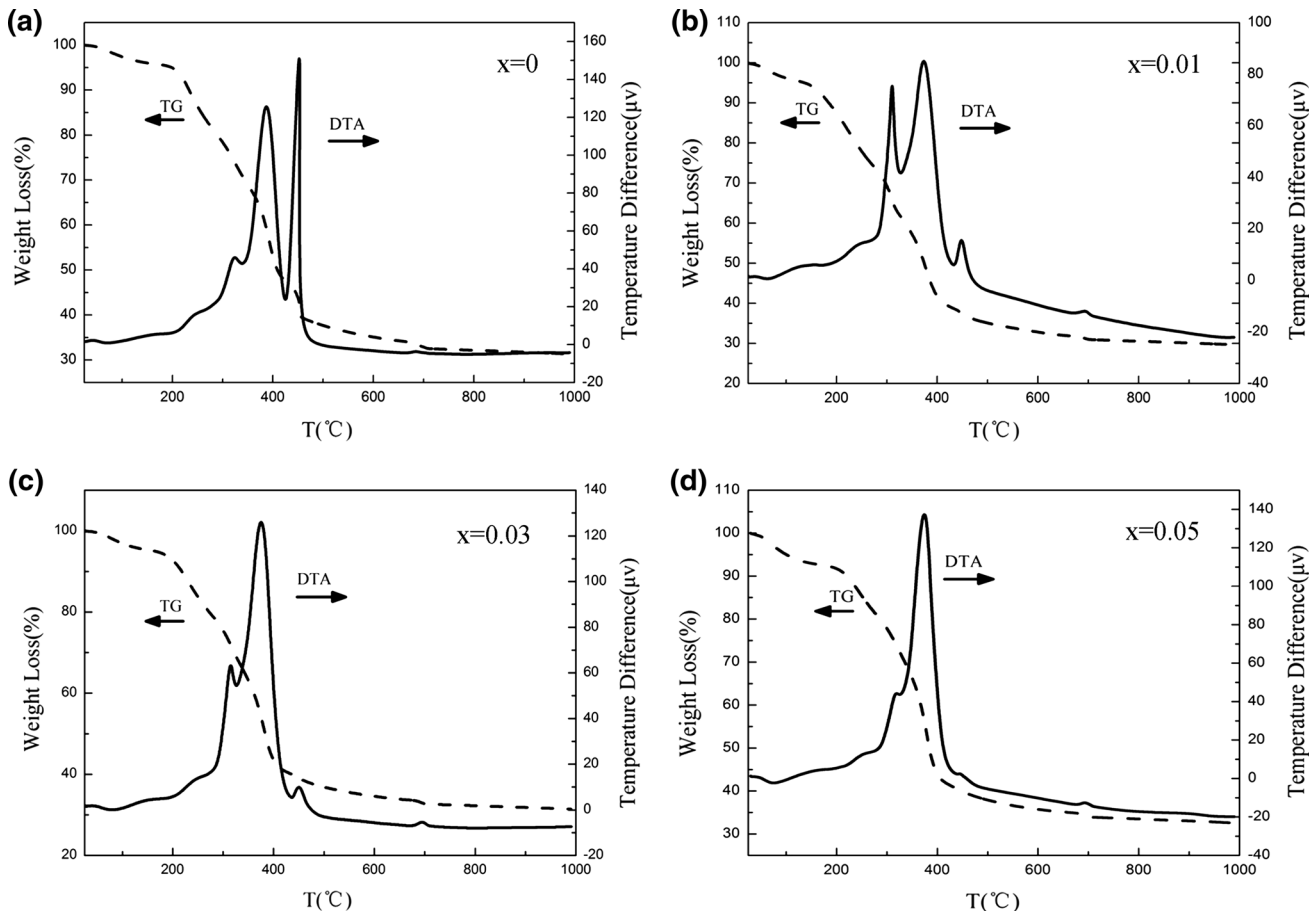

Fig. 2. TG-DTA curves of the $Ca_{0.9-x}Yb_xLa_{0.1}MnO_3$ ($0 \leq x \leq 0.05$) gels: (a) $x = 0$, (b) $x = 0.01$, (c) $x = 0.03$, and (d) $x = 0.05$.

an endothermic peak between 650 and 700°C occurred after the sharp weight loss, suggesting that there is a synthetic reaction taking place during the Ca$_{0.9-x}$Yb$_x$La$_{0.1}$MnO$_3$ generation process. Similar results have been found in previous studies.[17] After 900°C, there was no weight loss, indicating the formation of an oxide with a definite composition.

Phase Structure

Figure 3a and b shows the XRD patterns of the Ca$_{0.9-x}$Yb$_x$La$_{0.1}$MnO$_3$ powders calcined at 900°C and the ceramics sintered at 1300°C, respectively. It
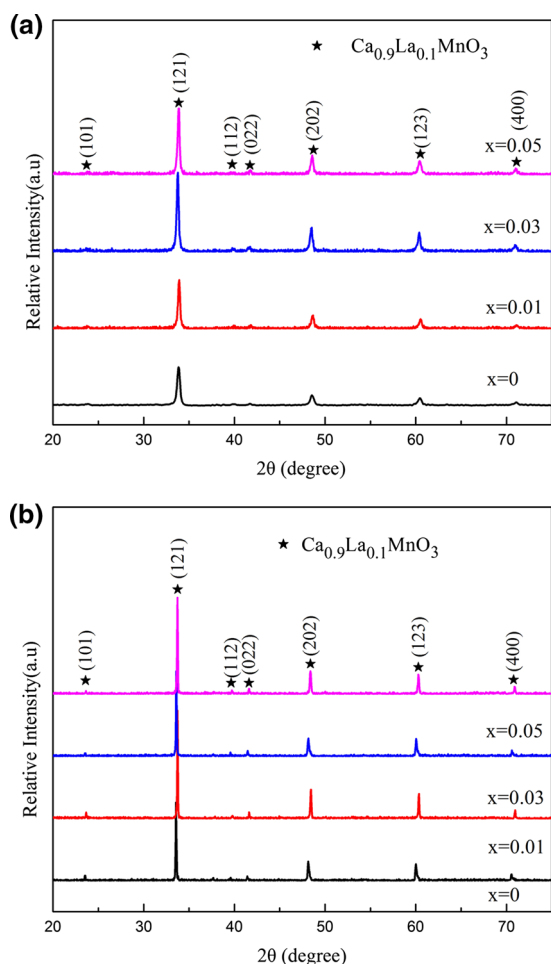

Fig. 3. XRD patterns of the calcined powders (a) and sintered ceramics (b) in the Ca$_{0.9-x}$Yb$_x$La$_{0.1}$MnO$_3$ (0 ≤ x ≤ 0.05) system.

can be seen that the diffraction peaks of all samples match well with an orthorhombic perovskite Ca$_{0.9}$La$_{0.1}$MnO$_3$ phase described by the space group *Pnma*. No secondary phase occurred with the increase of Yb concentration in both the calcined powders and sintered ceramics. This indicates that the Yb^{3+} ions have entered into the Ca$_{0.9}$La$_{0.1}$MnO$_3$ lattice, and the perovskite structures were formed completely at 900°C. This preparation temperature is much lower than that of the traditional solid state reaction. It can be seen that the diffraction peaks slightly shifted towards higher angles when the Yb was introduced in the Ca$_{0.9}$La$_{0.1}$MnO$_3$ samples, indicating that the unit cell volume decreases slightly. The structure was refined by using TOPAS. Lattice constants and cell volumes of the Ca$_{0.9-x}$Yb$_x$La$_{0.1}$MnO$_3$ ceramics are listed in Table I. A clear variation was observed in all parameters: a, b, c and cell volume decreased with increasing Yb content (Table I). This result can be understood based on the fact that the ionic radius of Yb^{3+} (0.087 nm) is smaller than that of Ca^{2+} (0.1 nm).

Microstructure

Figure 4 shows the SEM micrographs obtained from the surface of the Ca$_{0.9-x}$Yb$_x$La$_{0.1}$MnO$_3$ ceramics sintered at 1300°C. As can be seen, all ceramics had a relatively homogenous microstructure and were highly dense. The theoretical and experimental densities are summarized in Table I. The experimental density increased with increasing Yb content, which resultd from the large mass of the Yb element. The relative densities range from 97.04% to 98.65% of the theoretical density. The microstructure showed that there was no evident pore, which is consistent with the high relative density. It can be seen that the added Yb led to a slight increase in the grain size. This could be due to the fact that the Yb addition results in an increase in the grain boundary mobility and energy, which is beneficial to grain growth.[18] In addition, the average crystallite size of the Ca$_{0.9-x}$Yb$_x$La$_{0.1}$MnO$_3$ (x = 0, 0.01, 0.03, 0.05) ceramic samples by the Debye–Scherrer formulation are 62.9 nm, 67.6 nm, 80.8 nm, and 82.1 nm, respectively, indicating that the added Yb also led to a slight increase in crystallite size. A microstructure with spiral growth was also observed in these ceramics, especially for the

Table I. The lattice parameters, cell volumes, theoretical density, experimental density, relative density, and activation energy (E_a) of Ca$_{0.9-x}$Yb$_x$La$_{0.1}$MnO$_3$ (0 ≤ x ≤ 0.05) ceramics

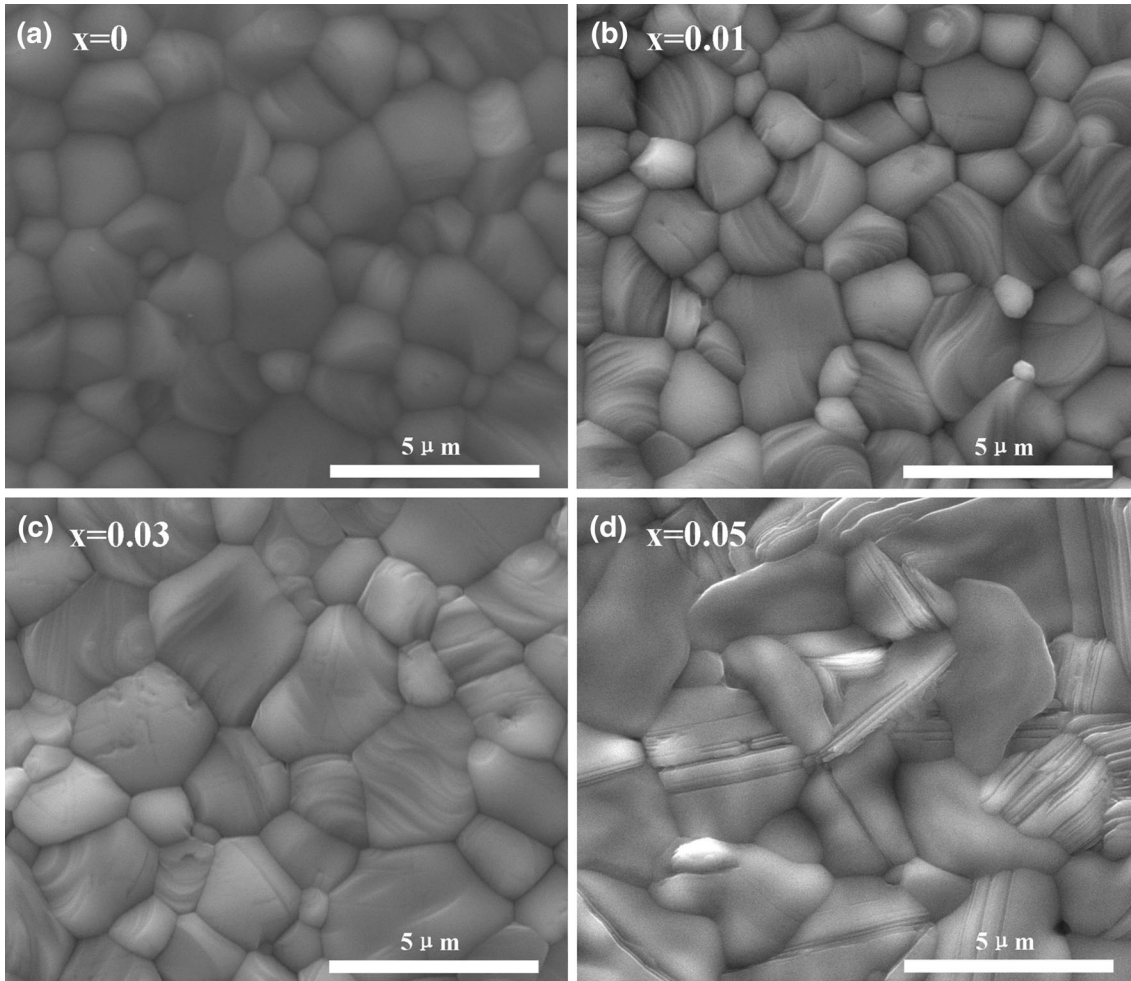| x	a (Å)	b (Å)	c (Å)	V (Å^3)	Theoretical density (g/cm^3)	Experimental density (g/cm^3)	Relative density (%)	E_a (meV)
0	5.3515 (2)	7.5662 (2)	5.3232 (6)	215.54 (3)	4.7136 (6)	4.5743	97.04	53.7
0.01	5.3435 (3)	7.5422 (2)	5.3199 (1)	214.40 (1)	4.7798 (2)	4.7154	98.65	50.7
0.03	5.3358 (5)	7.5308 (2)	5.3134 (6)	213.51 (3)	4.8825 (7)	4.8134	98.58	50.3
0.05	5.3156 (6)	7.5122 (3)	5.3108 (4)	212.07 (3)	4.9989 (7)	4.9030	98.08	47.9

Fig. 4. SEM images obtained from the surfaces of the $Ca_{0.9-x}Yb_xLa_{0.1}MnO_3$ ($0 \leq x \leq 0.05$) sintered ceramics: (a) $x = 0$, (b) $x = 0.01$, (c) $x = 0.03$, and (d) $x = 0.05$.

$x = 0.01$ and 0.03 samples. This spiral growth originates from the intergrowth of islands in the coalescence stage.[19] There was lamellar texturing observed in the specimen for $x = 0.05$, which is often detected in $Ca_3Co_4O_9$ ceramics.[20,21] This lamellar texturing is favorable toward improving TE properties.[20,21]

TE Properties

Figure 5 shows the temperature dependence of electrical resistivity, ρ, of the $Ca_{0.9-x}Yb_xLa_{0.1}MnO_3$ samples; the electrical resistivity increased with increasing temperature. Here, one can observe that the electrical resistivity decreased with an increase in the Yb content. The substituted manganate phase has a lower electrical resistivity compared to $CaMnO_3$ and can be modeled as a double exchange (DE) system coupled to the Jahn–Teller cation, Mn^{3+0}.[22] It is believed that electron-doped $CaMnO_3$ exhibits the hopping conductivity by electron hopping between Mn^{3+} and Mn^{4+}.[3,12,23–26] This mechanism can be described by the following equation[11]: $\rho = \rho_0 T \exp(E_a/kT)$, where E_a is the activation
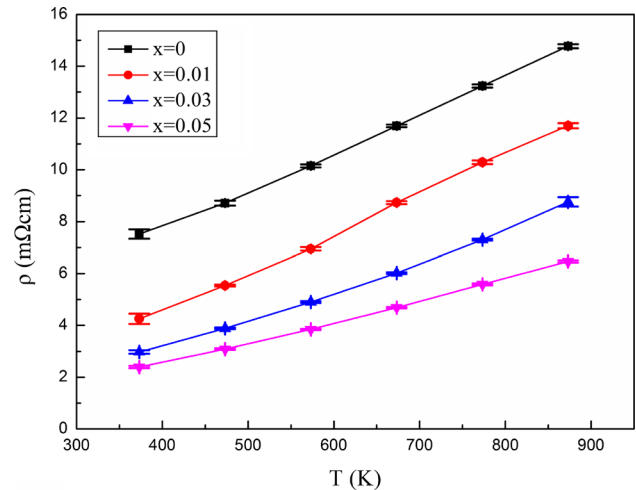

Fig. 5. Temperature dependence of electrical resistivity for $Ca_{0.9-x}Yb_xLa_{0.1}MnO_3$ ($0 \leq x \leq 0.05$) samples.

energy determined from the ρ measurement, ρ_0 is a constant, T is the absolute temperature, and k is the Boltzmann constant. The activation energy (Ea) for
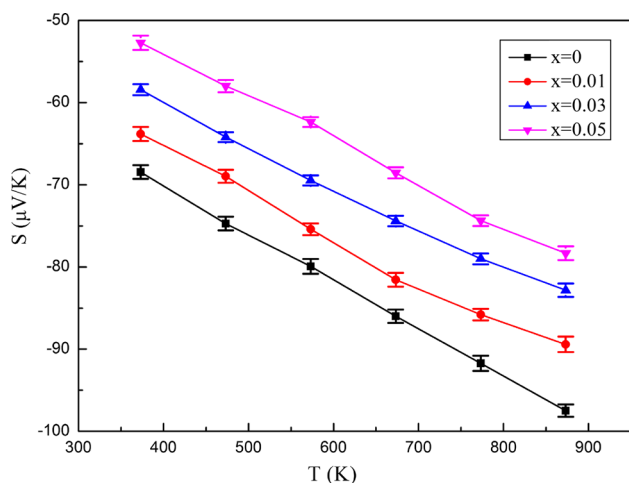
Fig. 6. Temperature dependence of the Seebeck coefficient for Ca$_{0.9-x}$Yb$_x$La$_{0.1}$MnO$_3$ ($0 \leq x \leq 0.05$) samples.

Fig. 7. Temperature dependence of power factor for Ca$_{0.9-x}$Yb$_x$La$_{0.1}$MnO$_3$ ($0 \leq x \leq 0.05$) samples.

electrical conduction has been calculated by using the temperature dependence of the electrical resistivity, and is listed in Table I. The activation energy Ea for pure Ca$_{0.9}$La$_{0.1}$MnO$_3$ is about 53.7 meV, which is in basic agreement with that reported in previous works (56.9 meV).[11,12] It can be seen that the Ea decreased as x increased. Thus, the decrease in ρ and Ea may result from the variation in electron concentration. On the basis of valence equilibrium, the substitution of Yb^{3+} for Ca^{2+} will increase Mn^{3+} and produce a large number of electron carriers, which can promote the electron hopping, thereby decreasing ρ as a result. The reduction in Ea should be attributed to the carrier's delocalization with the increase in Mn^{3+} concentration.[11] A more detailed discussion will be given in a later section.

The temperature dependence of thermopower, S, of the samples is shown in Fig. 6. Over the measured temperature range, the sign of S values is negative, indicating an n-type conduction and the major carrier is electrons. The absolute value of S for all the samples increased as the temperature rose. With the increase of Yb content, the absolute value of S decreased. In general, the thermopower is inversely proportional to the carrier concentration.[8,27] Therefore, the decreasing thermopower with the enhancement of the doping level in this system can also be evidence of an increase in the electron concentration due to the variation of the charge valance in accordance with the Verwey controlled ionic valance principle.[8,28]

From the measured values of ρ and S, the power factors P (=S^2/ρ) of the Ca$_{0.9-x}$Yb$_x$La$_{0.1}$MnO$_3$ samples were calculated, as shown in Fig. 7. The P for the Ca$_{0.9}$La$_{0.1}$MnO$_3$ sample increased at first, and then leveled off with the increase of temperature, similar to the previous results of Wang et al.;[12] however, the value of P was slight lower. These results may be mainly due to an increase in
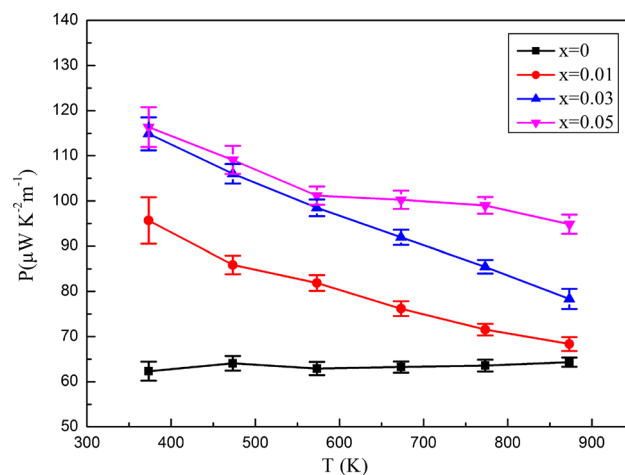
electrical resistivity, which is also larger than the values reported by the same authors.[12] These differences can be ascribed to the different microstructure caused by different preparation techniques and sintering process. Normally, the grain sizes produced through chemical methods are much smaller than those prepared by the solid state reaction method. With decreasing grain size, the interconnectivity between grains decreases, which reduces the possibility of electrons hopping to the neighboring sites, thereby increasing the electrical resistivity.[6,29] Similar results have been reported in previous research.[30] It can be seen that the power factor increased with increasing Yb content and obtained its maximum at $x = 0.05$, which can be ascribed to the significant decrease in electrical resistivity and a moderate decrease in the absolute value of the Seebeck coefficient. The power factor of the Yb-doped samples decreased with the increase of temperature, which is attributed to the evident rise of ρ and the slight increase of absolute value S with increasing temperature.

X-ray Photoelectron Spectroscopy Analysis

To further reinforce and support the above conclusion that electrical resistivity depends on the Yb substitution, the average Mn oxidation state was evaluated by XPS measurements. Figure 8 shows the XPS spectrum and the curve-fitting example of Ca$_{0.9-x}$Yb$_x$La$_{0.1}$MnO$_3$ in the region of Mn 2p core-level peaks. According to the binding energy values,[31] the Mn 2p peaks shown in Fig. 8 can be resolved into the contributions from Mn^{3+} and Mn^{4+}. The XPS results presented here are in agreement with the previous research[32,33] which showed the existence of two different Mn ions in this system, Mn^{3+} and Mn^{4+}. Quantitative data of the Mn 2p$_{3/2}$ spectra were obtained from the XPS results, and are shown in Table II. The ionic ratio of Mn^{3+}/Mn^{4+} was calculated by using the approximate relationship:
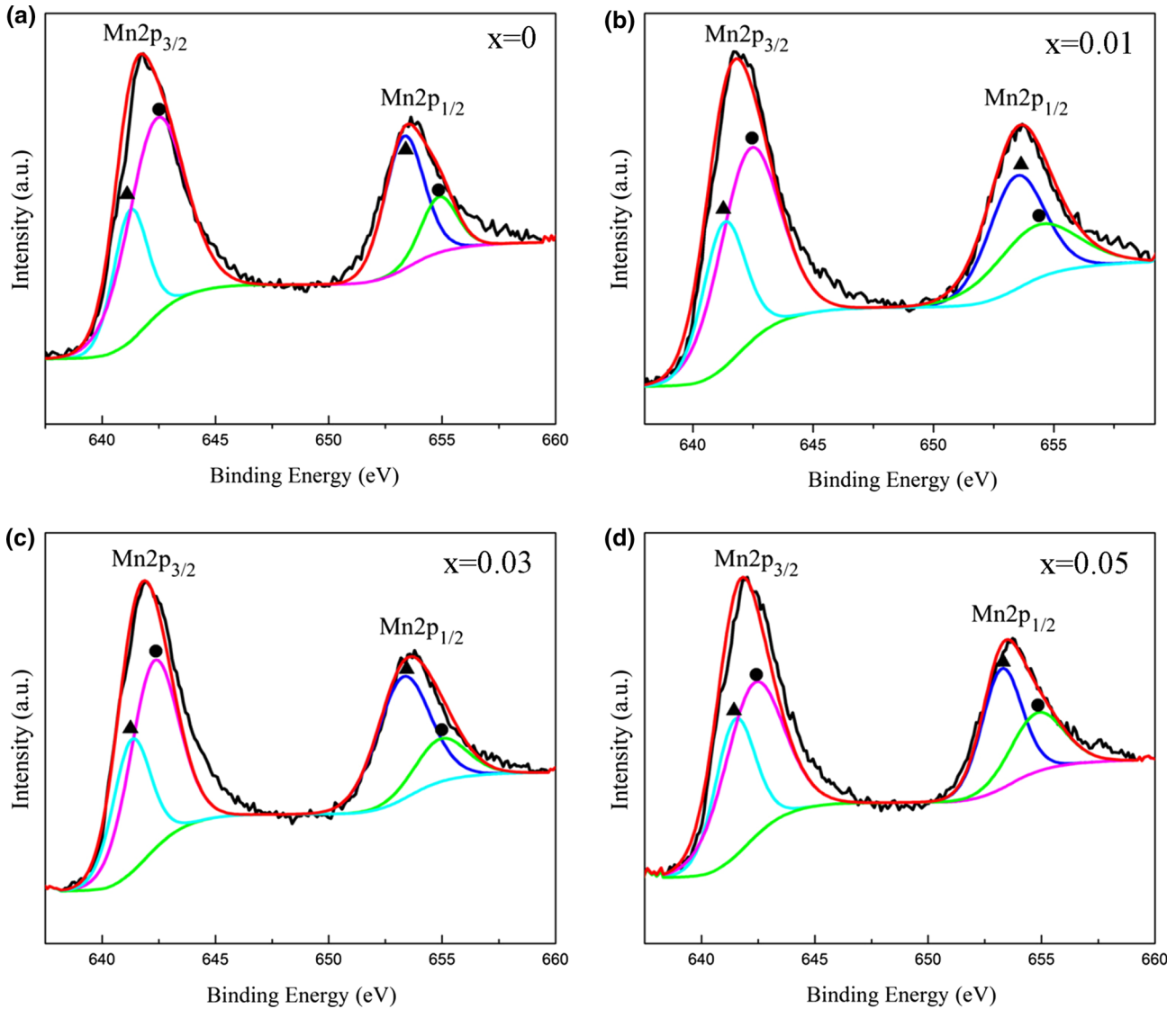
Fig. 8. XPS spectra of Mn 2p regions of $Ca_{0.9-x}Yb_xLa_{0.1}MnO_3$ ($0 \leq x \leq 0.05$) ceramics: (a) $x = 0$, (b) $x = 0.01$, (c) $x = 0.03$, and (d) $x = 0.05$. Triangle and filled circle indicate the peaks of the Mn 2p spectra attributed to Mn^{3+} and Mn^{4+}, respectively.

Table II. Mn $2p_{3/2}$ spectral fitting parameters: binding energy, peak area, ionic ratio of Mn^{3+}/Mn^{4+} and concentration of Mn^{3+}

x	Mn $2p_{3/2}$ binding energy (eV)		Mn $2p_{3/2}$ peak area		Ionic ratio of Mn^{3+}/Mn^{4+}	Mn^{3+} concentration (at.%)
	Mn^{4+}	Mn^{3+}	Mn^{4+}	Mn^{3+}		
0	642.39	641.24	38,720	15,344	0.3960	28.37
0.01	642.34	641.28	31,662	16,630	0.5249	34.42
0.03	642.28	641.30	31,161	17,159	0.5503	35.50
0.05	642.27	641.47	31,130	18,898	0.6068	37.76

$\frac{n_1}{n_2} = \frac{I_1}{I_2} \cdot \frac{\sigma_2}{\sigma_1} \left[\frac{Ek_2}{Ek_1} \right]^{1/2}$, where n_i, I_i, Ek_i, and σ_i are the number of atoms of element i, the XPS line intensity in terms of peak area, the kinetic energy value corresponding to the line considered, and the cross-section calculated theoretically, respectively.[34,35]

As mentioned above, the introduction of a trivalent cation such as Yb^{3+} generates Mn^{3+} cations in the Mn^{4+} matrix. The presence of Mn^{3+} greatly distorts the crystal structure accompanying the formation of Mn^{3+}–O–Mn^{4+} bonds due to the differences of ionic

radius between Mn^{3+} and Mn^{4+}.[36,37] Thus, the band structure and the carrier concentration vary with the extent of Yb substitution. The transport of charge carriers in manganate phases is mostly explained by the small polaron hopping model,[22,38,39] that is to say, the formation of polarons is defined as the combination of carriers with its strain field.[22] Thus, the resistivity decreases with increasing charge carrier concentration.[22] From Table II, it can be seen that the ionic ratio of Mn^{3+}/Mn^{4+} and the Mn^{3+} concentration increased with the increase of Yb content, which will lower the energy barriers for polaron hopping and increase the tendency to form small polarons, thus decreasing the electrical resistivity. Consequently, the added Yb enhances the electron concentration and electron hopping between Mn^{3+} and Mn^{4+}, thus decreasing the electrical resistivity, which is in accordance with our results (Fig. 5).

CONCLUSIONS

$Ca_{0.9-x}Yb_xLa_{0.1}MnO_3$ ceramics with a high relative density were successfully synthesized by the Pechini method. All samples show single phase with an orthorhombic perovskite structure. The added Yb leads to a slight increase in the grain size. Both the electrical resistivity and the absolute Seebeck coefficient decrease with the increase in Yb content. The power factor increases as the Yb content increases and obtains its maximum at $x = 0.05$. The electrical conduction in these compounds may be due to electron hopping between Mn^{3+} and Mn^{4+}, which is enhanced with increasing Yb content. Further work will be concentrated on the thermal conduction behavior and mechanism of this system, which could be an important class for obtaining a good TE material.

ACKNOWLEDGEMENTS

REFERENCES

1. Y. Wang, Y. Sui, H. Fan, X. Wang, Y. Su, W. Su, and X. Liu, *Chem. Mater.* 21, 4653 (2009).
2. G.J. Snyder and E.S. Toberer, *Nat. Mater.* 7, 105 (2008).
3. M. Ohtaki, H. Koga, T. Tokunaga, K. Eguchi, and H. Arai, *J. Solid State Chem.* 120, 105 (1995).
4. J.G. Noudem, D. Kenfaui, S. Quetel-Weben, C.S. Sanmathi, R. Retoux, and M. Gomina, *J. Am. Ceram. Soc.* 94, 2608 (2011).
5. Y. Wang, Y. Sui, X. Wang, W. Su, X. Liu, and H.J. Fan, *Acta Mater.* 58, 6306 (2010).
6. I. Matos, S. Sério, M. Lopes, M. Nunes, and M. Jorge, *J. Alloy Compd.* 509, 9617 (2011).
7. H. Taguchi, T. Kugi, M. Kato, and K. Hirota, *J. Am. Ceram. Soc.* 93, 3009 (2010).
8. S.M. Choi, C.H. Lim, and W.S. Seo, *J. Electron. Mater.* 40, 551 (2011).
9. J.F. Fergus, *J. Eur. Ceram. Soc.* 32, 525 (2012).
10. J. Lan, Y. Lin, A. Mei, C. Nan, Y. Liu, B. Zhang, and J. Li, *J. Mater. Sci. Technol.* 25, 535 (2009).
11. Y. Wang, Y. Sui, X. Wang, and W. Su, *J. Phys. D Appl. Phys.* 42, 055010 (2009).
12. Y. Wang, Y. Sui, and W. Su, *J. Appl. Phys.* 104, 093703 (2008).
13. S.G. Wang, A.M. Chang, H.M. Zhang, and Q. Zhao, *Mater. Chem. Phys.* 110, 83 (2008).
14. C. Silveira, M. Lopes, M. Nunes, and M. Jorge, *Solid State Ionics* 180, 1702 (2010).
15. M.A.L. Nobre and S. Lanfredi, *J. Phys. Chem. Solids* 64, 2457 (2003).
16. E. Asenath-Smith, I.N. Lokuhewa, S.T. Misture, and D.D. Edwards, *J. Solid State Chem.* 183, 1670 (2010).
17. X. Meng, S. Hao, J. Li, Q. Fu, and D. Fu, *Powder Technol.* 224, 96 (2012).
18. K. Park and J.K. Lee, *J. Alloy Compd.* 475, 513 (2009).
19. M.S. Ramachandra Rao, R. Pinto, S. Srinivas, and A.K. Bhatnagar, *Appl. Supercond.* 6, 11 (1998).
20. J.G. Noudem, *J. Eur. Ceram. Soc.* 29, 2659 (2009).
21. J. Noudem, D. Kenfaui, D. Chateigner, and M. Gomina, *J. Electron. Mater.* 40, 1100 (2011).
22. L. Bocher, M. Aguirre, D. Logvinovich, A. Shkabko, R. Robert, M. Trottmann, and A. Weidenkaff, *Inorg. Chem.* 47, 8077 (2008).
23. M. Melo Jorge, M. Nunes, R. Silva Maria, and D. Sousa, *Chem. Mater.* 17, 2069 (2005).
24. P. Isasi, M. Lopes, M. Nunes, and M. Melo Jorge, *J. Phys. Chem. Solids* 70, 405 (2009).
25. S.H. Chun, M.B. Salamon, Y. Lyanda-Geller, P.M. Goldbart, and P.D. Han, *Phys. Rev. Lett.* 84, 757 (2000).
26. G. Jakob, W. Westerburg, F. Martin, and H. Adrian, *Phys. Rev. B* 58, 14966 (1998).
27. J.P. Heremans, V. Jovovic, E.S. Toberer, A. Saramat, K. Kurosaki, A. Charoenphakdee, S. Yamanaka, and G.J. Snyder, *Science* 321, 554 (2008).
28. E. Verwey, P. Haaijman, F. Romeijn, and G. Van Oosterhout, Controlled-valency semiconductors. *Philips Res. Rep.* 5, 173 (1950).
29. A. Banerjee, S. Pal, S. Bhattacharya, B. Chaudhuri, and H. Yang, *J. Appl. Phys.* 91, 5125 (2002).
30. K. Park, *J. Am. Ceram. Soc.* 88, 862 (2005).
31. T. Hashemi and A. Brinkman, *J. Mater. Res.* 7, 1278 (1992).
32. T. Taniguchi, S. Mizusaki, N. Okada, Y. Nagata, S. Lai, M. Lan, N. Hiraoka, M. Itou, Y. Sakurai, and T. Ozawa, *Phys. Rev. B* 77, 014406 (2008).
33. S. Estemirova, A. Fetisov, and V. Fetisov, *J. Appl. Spectrosc.* 76, 394 (2009).
34. Y. Boudeville, F. Figueras, M. Forissier, J.-L. Portefaix, and J.C. Vedrine, *J. Catal.* 58, 52 (1979).
35. F. Guan, H. Zhang, A. Chang, P. Zhao, and B. Zhang, *J. Mater. Sci. Mater. Electron.* 23, 1728 (2012).
36. D. Flahaut, T. Mihara, R. Funahashi, N. Nabeshima, K. Lee, H. Ohta, and K. Koumoto, *J. Appl. Phys.* 100, 084911 (2006).
37. P. Liang, Z. Yang, X. Chao, and Z. Liu, *J. Am. Ceram. Soc.* 95, 2218 (2012).
38. J. Hejtmanek, Z. Jirak, M. Maryško, C. Martin, A. Maignan, M. Hervieu, and B. Raveau, *Phys. Rev. B* 60, 14057 (1999).
39. A. Maignan, C. Martin, F. Damay, B. Raveau, and J. Hejtmanek, *Phys. Rev. B* 58, 2758 (1998).